Chapter 4

Results of Analysis of Helioseismic Data

There are two main results in this chapter, which uses helioseismology data from MDI, GONG, and BBSO. The first result is that near-pole rotation is slower than one would expect from a smooth extrapolation of the rotation rate at lower latitudes and furthermore the near-pole rotation rate changes with time. The second result is a possible detection of longitudinal structures in the convection zone. The interpretation of these structures is difficult because of the possible contamination of the signal by surface magnetic field.

This chapter contains three sections. The first, section 4.1, is a brief introduction to inverse problems in helioseismology. The following section, 4.2, describes the results of the inversions of frequency splittings for rotation rate in the upper convection zone. The final section, 4.3, concerns the inversion of travel times for large-scale longitudinal structure over three Carrington rotations.

4.1 An Introduction to Inversions

The process of inferring information about subsurface conditions from helioseismic data consists of two steps. The first is to solve the forward problem, i.e. to determine how the observed data depend on the parameters of the solar model. The second step is the inverse problem, using the observed data to infer the parameters of the

model. The forward problem for time-distance helioseismology was discussed in some detail in the previous chapter. This chapter concerns itself with the results of inversions of real data. As a result, a small introduction to the practicalities of doing inversions is in order.

In this introduction I will consider only inversions using the method of Optimally Localized Averages (OLA), pioneered in the field of geophysics by Backus & Gilbert (1968). The other main method in use in helioseismology is Regularized Least Squares (RLS). In this section I will discuss only the one-dimensional problem; the OLA method in higher dimensions is not conceptually any different. The problem that we want to solve is of the form

$$d_i = \int \mathrm{d}x \; K_i(x) f(x) \,. \tag{4.1}$$

The data are d_i, the kernels are $K_i(x)$, and the unknown function that we want to estimate is $f(x)$. The integral over x is a spatial integral; it could in general be in more than one dimension.

The OLA method consists of writing the estimate of the function f at a particular value of x as a linear combination of the data values

$$\tilde{f}(x_j) = \sum_i a_{ij} d_i \,. \tag{4.2}$$

The estimate of f at the point x_j is denoted by $\tilde{f}(x_j)$. By inserting equation (4.1) into the above equation we obtain

$$\tilde{f}(x_j) = \int \mathrm{d}x \; \kappa_j(x) f(x) \,, \tag{4.3}$$

with the averaging kernels $\kappa_j(x)$ given by

$$\kappa_j(x) = \sum_i a_{ij} K_i(x) \,. \tag{4.4}$$

The essential process in OLA inversion is to choose the coefficients a_{ij} so that the averaging kernels $\kappa_j(x)$ are localized around x_j. This can be carried out by minimizing

a function of the form

$$\chi^2 = \int \mathrm{d}x\, W(x - x_j)\kappa_j^2(x) + \alpha \sum_i a_{ij}^2 \sigma_i^2 \,. \tag{4.5}$$

The function $W(x - x_j)$ is an arbitrary weight function, a common choice being $W(x) = x^2$. The first term in χ^2 penalizes the averaging kernels for being large where the weight function is large, i.e. far from x_j. The second term controls the error magnification; the σ_i are the error estimates for each of the data points d_i. The "regularization parameter", α, is a free parameter in the OLA approach and controls the balance between localized kernels and large errors.

4.2 Subsurface Rotation from MDI, GONG, and BBSO [1]

In this section we focus on latitudinal differential rotation, radially averaged over the outer 30 Mm of the convection zone, using SOI-MDI, GONG, and BBSO data. The advantage of a one-dimensional method is that what is sacrificed in radial resolution is gained in latitudinal resolution. Therefore, this analysis is a useful complement to two-dimensional inversions.

4.2.1 The Data

The data used in this analysis consist of the frequencies of p-mode solar oscillations as measured by SOI-MDI (Solar Oscillations Investigation - Michelson Doppler Imager), described by Scherrer et al. (1995), GONG (Global Oscillations Network Group), described by Harvey et al. (1996), and BBSO (Big Bear Solar Observatory), described by Woodard & Libbrecht (1993). Two 72-day averaged data sets from SOI-MDI are considered. The first runs from May 1 to July 12,1996 and the second from July 12 to September 22,1996 (hereafter called MDI A and MDI B data

[1] *This section is a combination of an ApJ Letter (Birch & Kosovichev, 1998a) and a proceedings paper (Birch & Kosovichev, 1998b). I carried out the analytical and numerical work, except for the calculation of the radial dependence of the frequency splitting kernels, and wrote the papers. The frequency splitting data were provided by the SOI-MDI, GONG, and BBSO experiments.*

sets respectively). Each SOI-MDI data set is a set of 36 coefficients a_{nl}^k for each observed n, l pair that can be used to obtain approximate frequencies for individual modes

$$\omega_{nlm} - \omega_{nl} = \sum_{k=1}^{36} a_{nl}^k P_k^l(m) \tag{4.6}$$

where ω_{nl} is the mean frequency of the multiplet and the P_k^l are orthogonal polynomials, first described by Ritzwoller and Lavely (1991).

One data set from the GONG experiment is used; it represents the average of the data from June 6 to September 21,1996. The data consist of frequencies for individual modes, which are used to calculate splittings for individual modes.

Four data sets from BBSO are used; they are the one year averages for 1986, 1988, 1989, and 1990. The data are sets of coefficients a_{nl}^k that are used to approximate individual mode frequencies:

$$\omega_{nlm} - \omega_{nl} = L \sum_{k=1}^{12} a_{nl}^k P_k(\frac{m}{L}) \tag{4.7}$$

where $L^2 = l(l+1)$ and P_k are Legendre polynomials of order k. (Woodard & Libbrecht, 1993).

For this work only modes with radial turning point above $.95 R_\odot$ are used; this is done in order to maintain some radial resolution. In addition modes with frequencies below 1.5 mHz or above 3.5 mHz are discarded as the splittings and errors are less certain there.

4.2.2 Inversion Method

Frequency splitting is given approximately (e.g. Sekii, 1997) by

$$\Delta\omega_{nlm} = \int_0^{\frac{\pi}{2}} \int_0^{R_\odot} \Omega(r,\theta) K_{nlm}(r,\theta)\, \mathrm{d}r\, \mathrm{d}\theta \tag{4.8}$$

with

$$K_{nlm}(r,\theta) = K_{nl}(r) W_{lm}(\theta) + L_{nl}(r) X_{lm}(\theta) \tag{4.9}$$

where $\Omega(r,\theta)$ is the symmetric part of the rotation rate, r is the radial coordinate, and θ is colatitude. Sekii (1997) also argues that the second term in the kernel is much smaller than the first; thus in this work only the first term is used. Because the mode kernels are even in latitude, frequency splitting is only sensitive to the part of the rotation law that is North-South symmetric.

In order to reduce noise the data are averaged before the inversion is performed. The asymptotics of the problem, which apply to the frequency splittings corrected for the effect of the Coriolis force by dividing by

$$\beta_{nl} \equiv \int_0^{R_\odot} K_{nl}(r)\,\mathrm{d}r\,, \tag{4.10}$$

are used to suggest an effective averaging technique. For $l \gg 1$, $\Delta\omega_{nlm}/\beta_{nl}$ is approximately a function of only the radial and angular turning points of the mode characterized by nlm, which describe the region where the mode eigenfunction is significant (e.g. Kosovichev & Parchevsky, 1988). We first correct the frequency splittings by dividing them by β_{nl}. We then discard all modes with radial turning points below $0.95R_\odot$. Finally we average all of the corrected frequency splittings with similar latitudinal turning points. In this work we use $N = 50$ equally sized bins in latitudinal turning point.

The averaged corrected frequency splitting, defined by

$$\tilde{\Delta\omega}_i \equiv \left\langle \frac{\Delta\omega_{nlm}}{\beta_{nl}} \right\rangle_i\,, \tag{4.11}$$

then obeys

$$\tilde{\Delta\omega}_i = \int_0^{\frac{\pi}{2}} \int_0^{R_\odot} \Omega(r,\theta) \left\langle W_{lm}(\theta) \frac{K_{nl}(r)}{\beta_{nl}} \right\rangle_i \mathrm{d}r\,\mathrm{d}\theta\,, \tag{4.12}$$

where $i = 1, 2, ...N$ and the angle brackets denote the average, weighted by the inverse square of the error in the mode frequency splitting, in the i^{th} bin. This approximation so far would not be useful, but the averaged kernels are approximately separable in r and θ, so that the average of the kernels can be written as the product of the separate averages of the functions $K_{nl}(r)$ and $W_{lm}(\theta)$

$$\left\langle W_{lm}(\theta) \frac{K_{nl}(r)}{\beta_{nl}} \right\rangle_i \simeq \left\langle W_{lm}(\theta) \right\rangle_i \left\langle K_{nl}(r)/\beta_{nl} \right\rangle_i = W_i(\theta) K_i(r)\,. \tag{4.13}$$

This is expected from the asymptotics, as all of the modes that are averaged together in a particular bin have similar angular turning points and thus kernels with similar angular dependence. With the notation

$$\overline{\Omega}_i(\theta) = \int_0^{R_\odot} \Omega(r,\theta) K_i(r)\,\mathrm{d}r \tag{4.14}$$

and the observation that $\overline{\Omega}_i(\theta)$, which is the radial average of the rotation rate for each kernel $K_i(r)$, is approximately independent of i, which will be demonstrated later, the above equation reduces to

$$\tilde{\Delta\omega}_i = \int_0^{\frac{\pi}{2}} W_i(\theta)\overline{\Omega}(\theta)\,\mathrm{d}\theta\,. \tag{4.15}$$

The Optimally Localized Averaging (OLA) inversion technique (Backus & Gilbert, 1968) is then applied to the integral equation. For each target location θ_0, coefficients $a_i(\theta_0)$ are computed such that

$$\chi^2 = \sum_{i=1}^{N} \int_0^{\frac{\pi}{2}} (\theta-\theta_0)^2 a_i(\theta_0) W_i(\theta)\,d\theta + \alpha \sum_{i=1}^{N} \left[a_i(\theta_0)\sigma_i\right]^2 \tag{4.16}$$

is minimum. Here σ_i is the formal error on the i^{th} frequency splitting average. The rotation rate, averaged over both depth and latitude, $\tilde{\Omega}(\theta_0)$ is then given by

$$\tilde{\Omega}(\theta_0) = \sum_i a_i(\theta_0)\tilde{\Delta\omega}_i\,. \tag{4.17}$$

The trade-off between localized averaging and the formal error of the result is controlled by the choice of α. For this work α was chosen to be a constant which provides sufficiently smooth inversions and reasonable error estimates independent of data set and θ_0.

4.2.3 Averaging Kernels

The result of the OLA inversion technique, $a_i(\theta_0)$, can be converted to a set of coefficients $c_{nlm}(\theta_0)$ such that the inferred radially and latitudinally averaged rotation

rate at a latitude θ_0 is

$$\tilde{\Omega}(\theta_0) = \sum_{nlm} c_{nlm}(\theta_0)\Delta\omega_{nlm} \,. \tag{4.18}$$

The averaging kernels, $\kappa(r, \theta; \theta_0)$, which satisfy

$$\tilde{\Omega}(\theta_0) = \int_0^{\frac{\pi}{2}} \int_0^{R_\odot} \kappa(r, \theta; \theta_0)\Omega(r, \theta)\, \mathrm{d}r\, \mathrm{d}\theta \tag{4.19}$$

are thus given by

$$\kappa(r, \theta; \theta_0) = \sum_{nlm} c_{nlm}(\theta_0) K_{nl}(r) W_{lm}(\theta) \,. \tag{4.20}$$

The averaging kernels are peaked in θ and very broad in r. Because the kernels are sharply peaked in θ they are approximately separable.

For a given data set, all of the averaging kernels have very similar radial dependence, as in seen in Figure 4.1. The radial dependence of the kernels shows that what is calculated by this inversion technique is the rotation rate averaged over the region shallower than about $0.96R_\odot$. The latitudinal dependence of the averaging kernels for the different data sets is shown in Figure 4.2. For all of the data sets the kernels are localized for each target position, and for targets away from the poles and the equator are sharply peaked.

4.2.4 Testing on Artificial Data

The method was first tested against the artificial data set `test2` described by Schou et al. (1998). First the artificial data was run through the inversion procedure. The artificial rotation law was then radially, but not latitudinally, averaged using the latitudinally integrated averaging kernels.

Figure 4.3 shows a comparison of the inversion result with the radial averages of the artificial rotation rate. The radial averages, one for each target location, are similar, which shows that the variation with θ_0 of the depth dependence of the averaging kernels will not significantly affect the latitudinal dependence of the inversion result. In addition the inversion results are very close to the expected radial averages of the rotation rate. Formally, one should compare the inversion result with the latitudinal as well as radial average of the rotation rate. In this

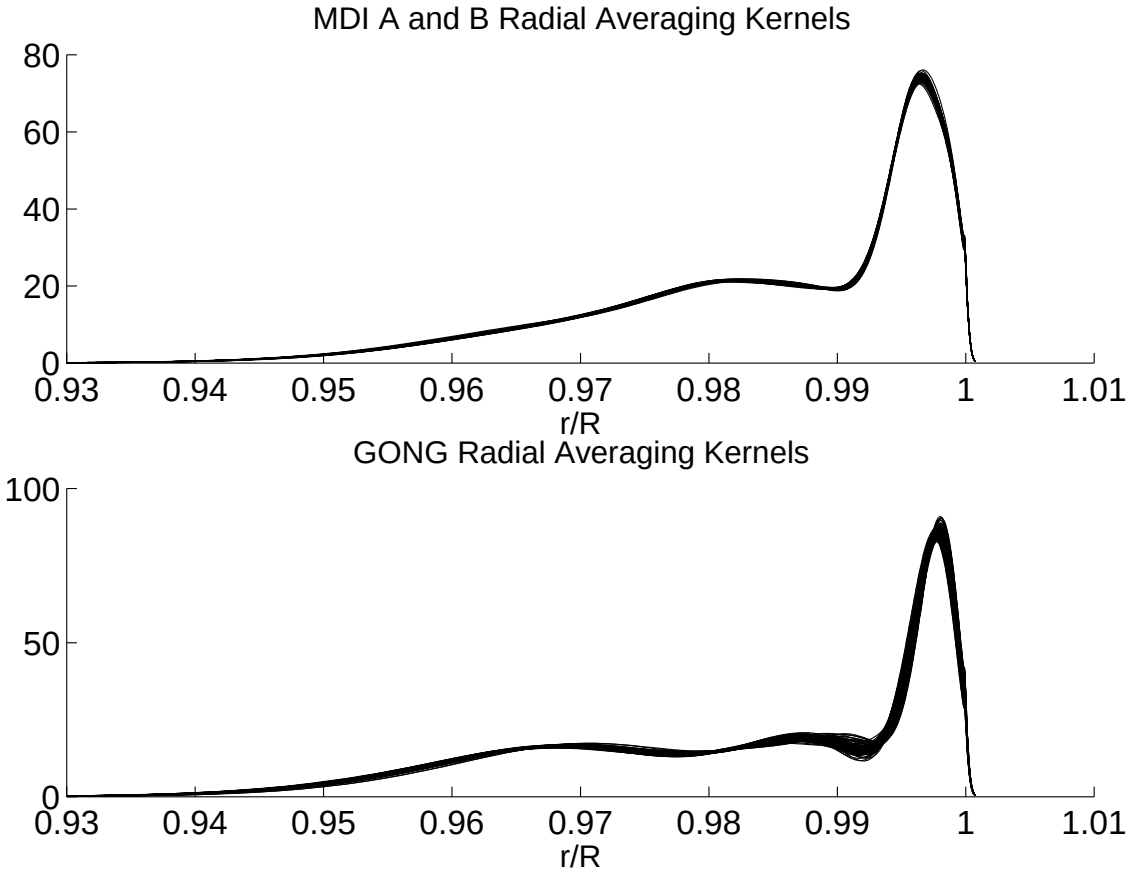

Figure 4.1: Latitudinally integrated averaging kernels for all target locations for the SOI-MDI and GONG data sets. The radial dependence of the averaging kernels is similar for all target locations within a data set, and quite similar from one data set to the next. The averaging kernels for the inversion of the GONG data have slightly more weight than those for the MDI data in the range $0.96R_\odot < r < 0.98_\odot$ and correspondingly less for $0.98R_\odot < r < 0.99R_\odot$.

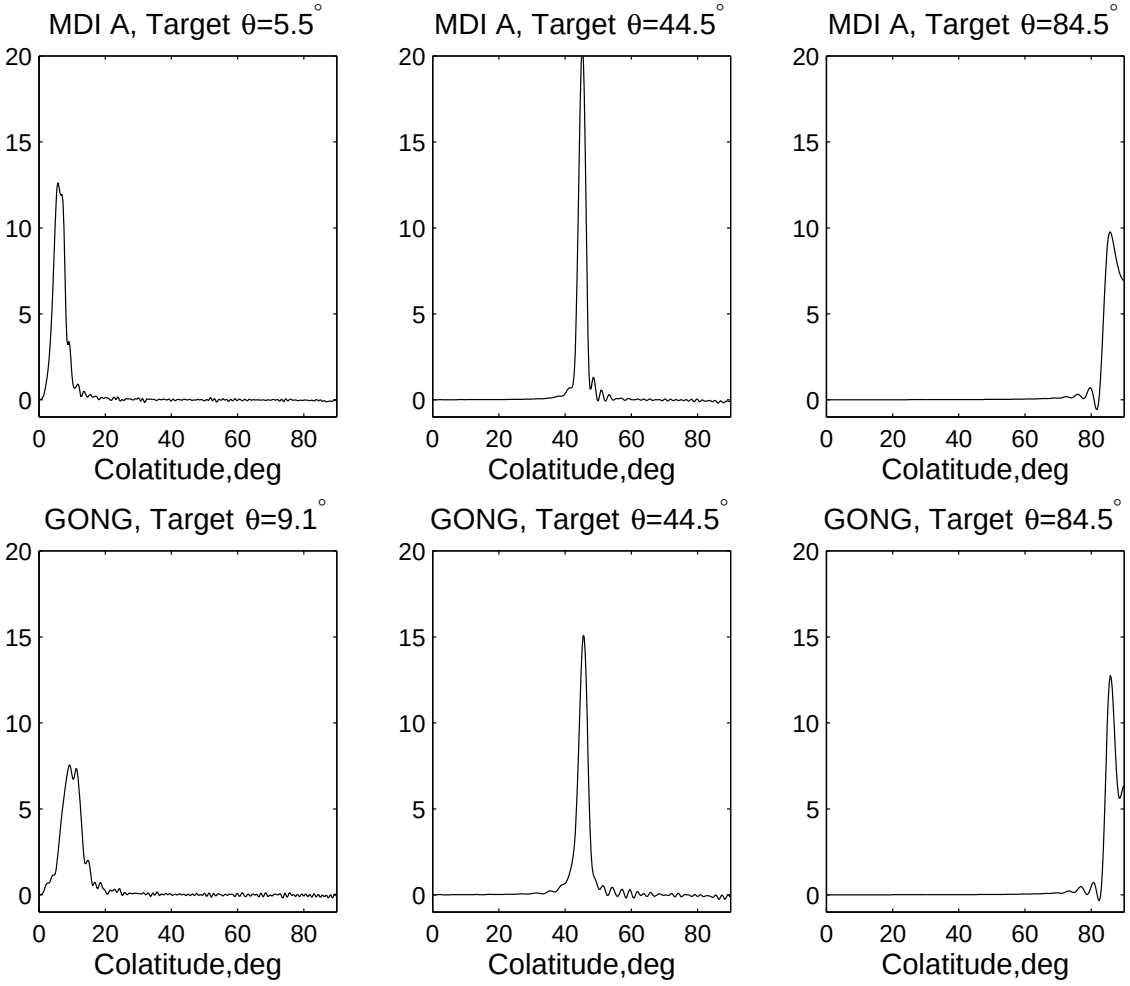

Figure 4.2: The latitudinal dependence of the averaging kernels. The top row is for the MDI A data set, the bottom row for the GONG data set. The kernels from the MDI A and B data sets are indistinguishable. The left column shows the kernels nearest the pole and the right shows the kernels closest to the equator. The kernels are localized in all cases.

particular study, however, the latitudinal averaging is not important.

4.2.5 Results from MDI, GONG, and BBSO

The result of the OLA method applied to the MDI and GONG data sets is shown in Figure 4.4. The three inversion results, which are approximately the average of the rotation rate for $0.96R_\odot < r < R_\odot$, are essentially the same to within the formal errors.

In order to further compare the results, a separate three-term fit in even powers of $\cos\theta$, as discussed in the introduction, is removed from each curve. This smooth component is removed in order to reveal the smaller scale features of the rotation rate. The fitting is done by changing coordinates to $x = \cos\theta$ and then doing a least squares fit, ignoring the horizontal error bars on the inversion, to a 4^{th} degree even polynomial in x. The results are shown in Figure 4.5. All three data sets show a negative residual near the pole.

In addition to the large feature near the pole there is also evidence, shown in Figure 4.6, for zonal flows. The flows have an amplitude of a few m/s and have a spatial scale of 10° to 20°. These flows have been seen previously in the SOI-MDI data (Kosovichev & Schou, 1997; Schou et al., 1998). The presence of zonal flows in the inversion of the GONG data shows that the higher a coefficients calculated from the GONG frequency splittings contain some information about the rotation rate. In particular it appears that the GONG data should have enough latitudinal resolution to see the elusive high latitude jet seen by RLS inversions of SOI-MDI data (Schou et al., 1998).

Figure 4.7 shows the OLA inversions of the four BBSO data sets. The regularization parameter α has been chosen to favor small formal errors at the expense of latitudinal resolution. This is done in order make variations from one data set to the next clearer.

Time variation in the BBSO data has been studied before (e.g. Gough & Stark, 1993; Woodard & Libbrecht, 1993). Woodard and Libbrecht (1993) used an asymptotic inversion method to infer the depth-averaged rotation rate as a function of latitude. Their work showed a change in the rotation rate at 30° colatitude of about 5 nHz from 1986 to 1990, with smaller changes elsewhere. The averaging kernels for

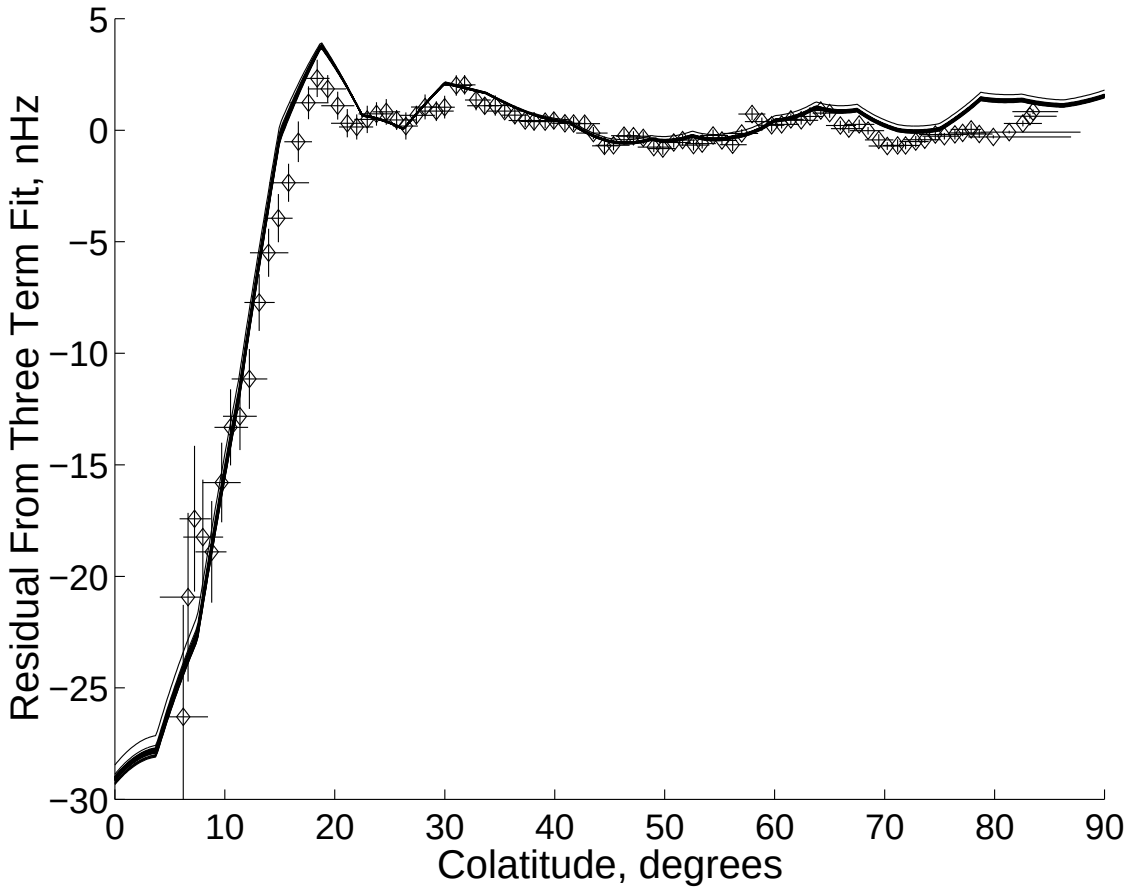

Figure 4.3: Comparison between the inversion of the artificial data and the radial averages of the artificial rotation rate. The inversion result is indicated by the diamonds with error bars. The horizontal error bars indicate the half-width at half-maximum to the left and right of the peak. The vertical error bars indicate the formal uncertainty in the average rotation at that target location (Gough, 1996). The diamonds are plotted at the centers of gravity of the radially integrated averaging kernels. The radial averages are indicated by the solid lines, one for each target location. The radial averaging is done with the latitudinally integrated averaging kernels.

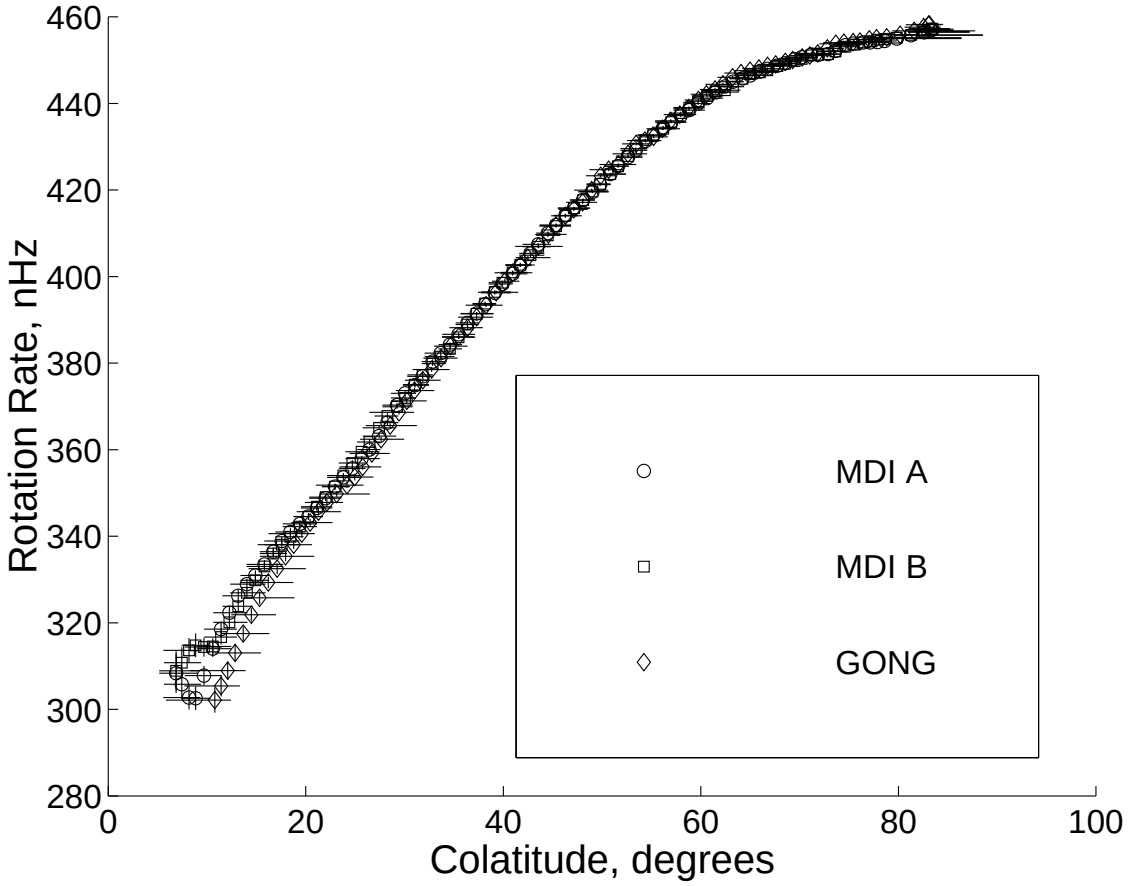

Figure 4.4: Rotation profiles obtained by OLA inversion of the MDI and GONG data sets. The results agree to within the formal errors. The GONG data gives a rotation rate that is systematically, but not significantly, lower than the SOI-MDI in the region closer than 20° to the pole.

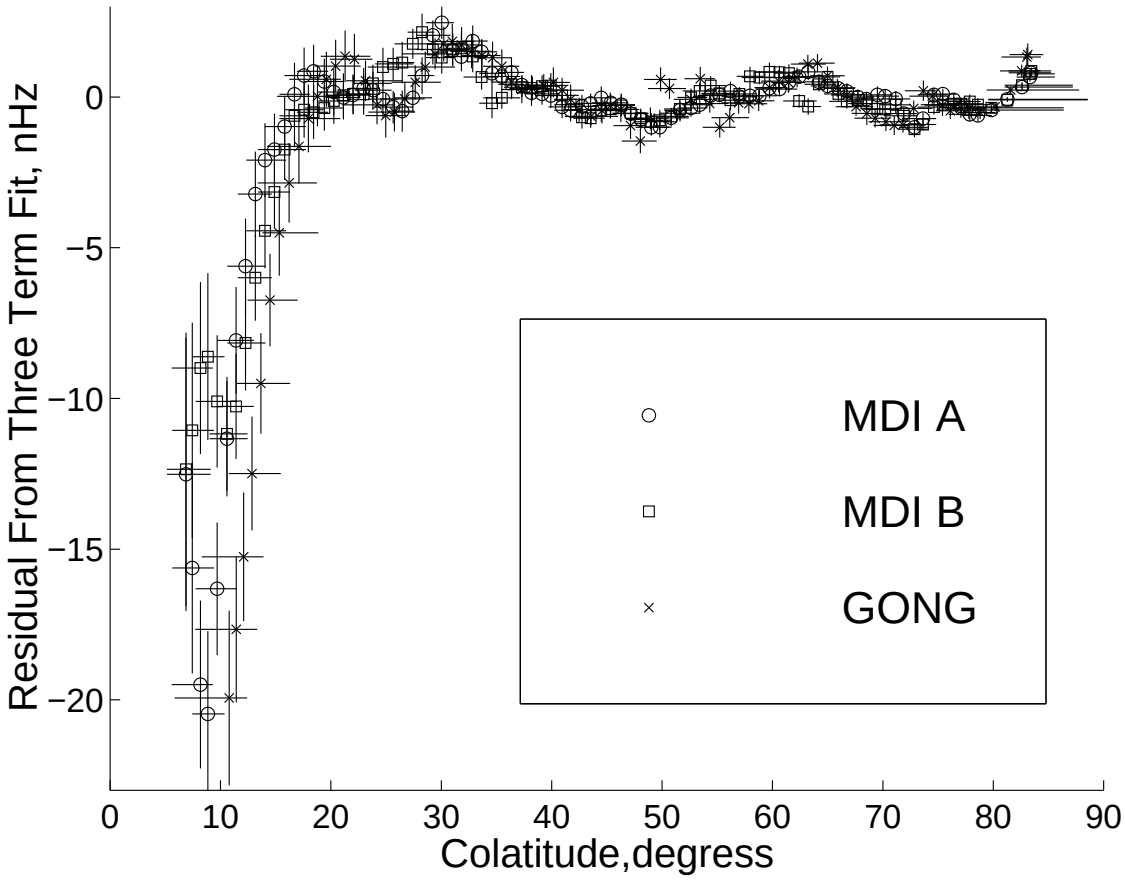

Figure 4.5: The residuals of the inversion results (Fig. 4.4) from three-term fits in even powers of $\cos\theta$. All three results show a sharp deviation from the three-term law at roughly 20° as well as small zonal flows.

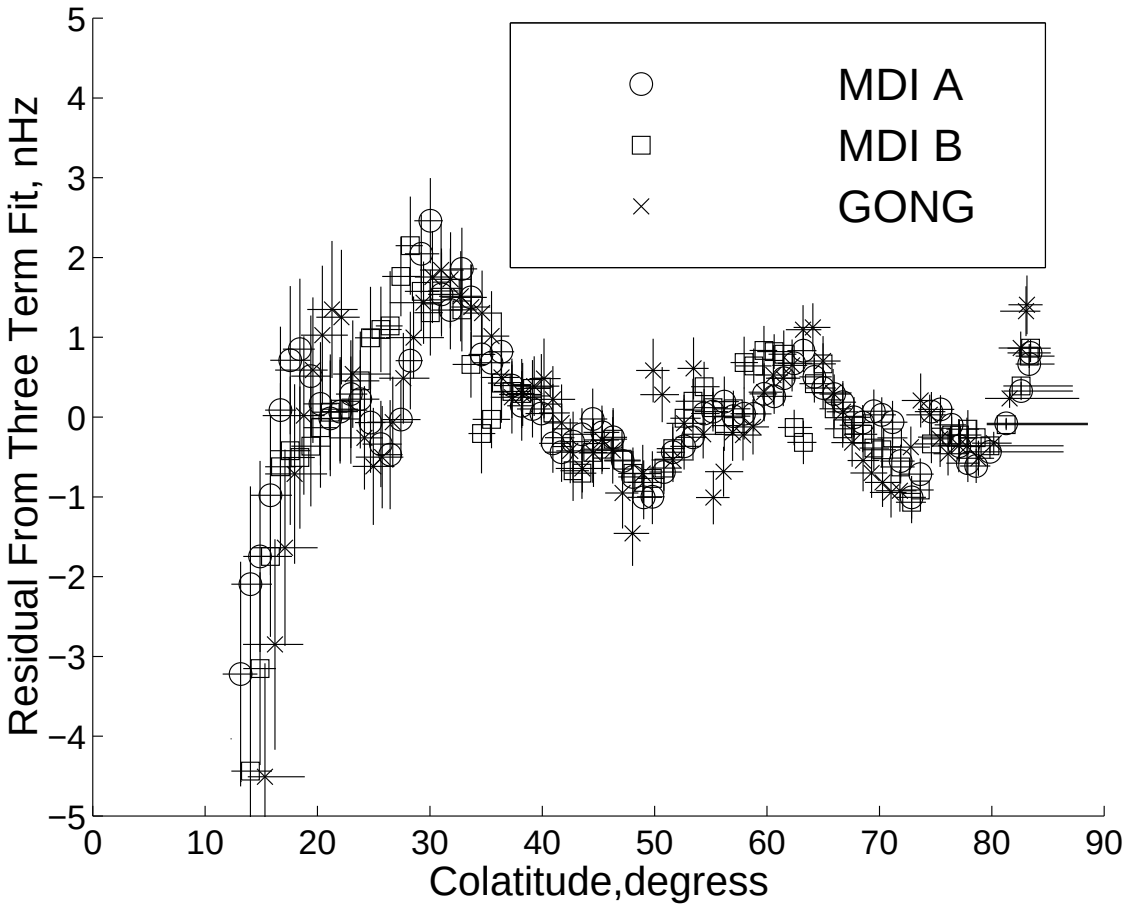

Figure 4.6: The deviation of the inversions from separate three term fits. Zonal flows are clearly seen.

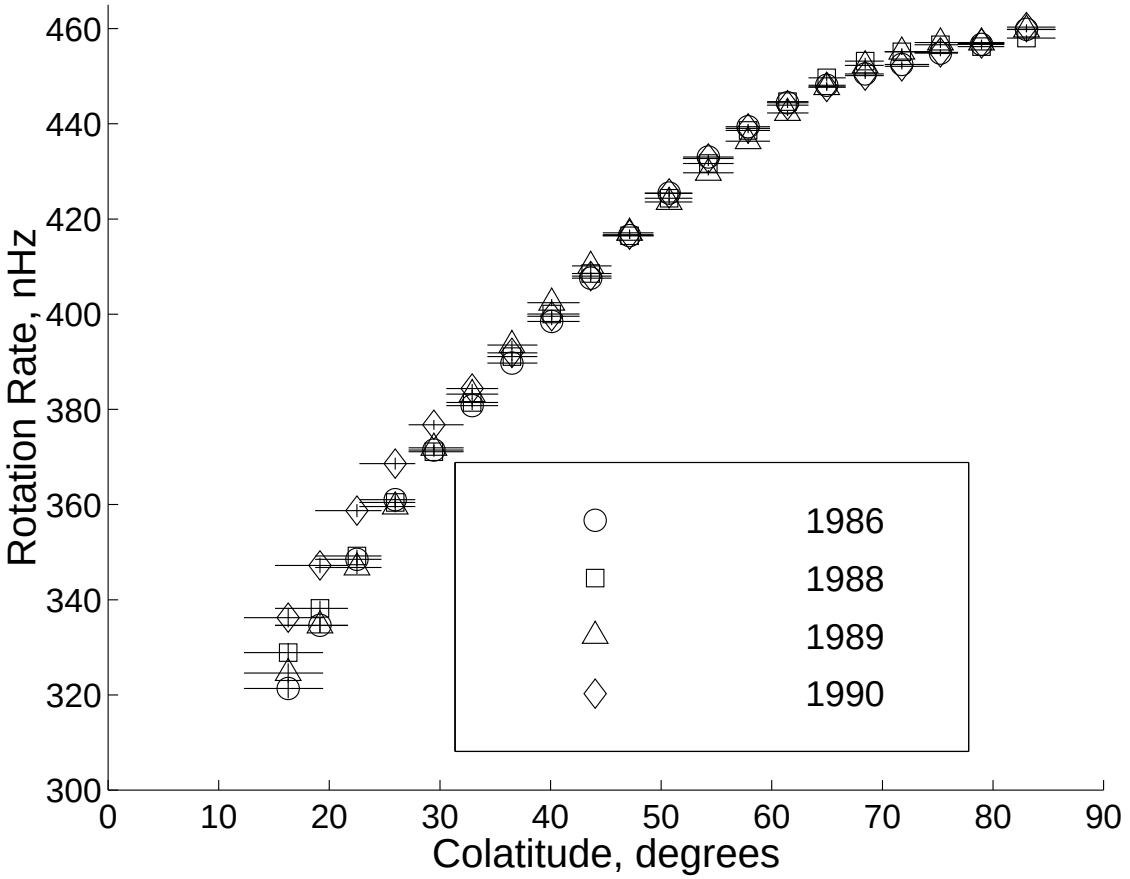

Figure 4.7: OLA inversions of the four different BBSO data sets. The regularization parameter α was chosen to favor small formal errors in the inversion at the expense of latitudinal resolution. This was done to make variations from one data set to the next more visible.

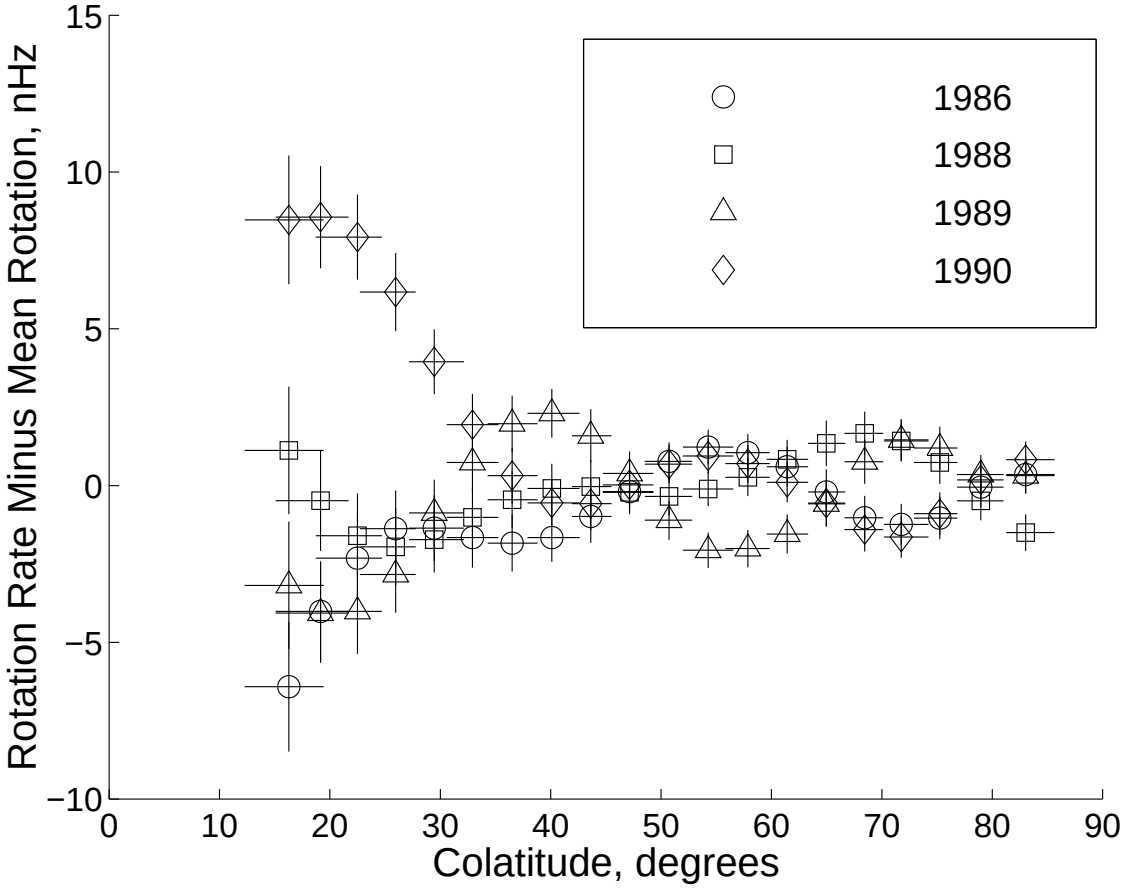

Figure 4.8: Deviations of the inversions of the BBSO data from the mean rotation. Solar minimum was near 1986 and maximum near 1990. The inferred rotation rates suggest that the rotation was less differential at maximum.

the asymptotic method they employed are not well localized so the exact latitude may not be correct, but the result does indicate some year to year variation in the BBSO data.

In order to make differences from one year to the next more clear Figure 4.8 shows the same inversion results except with the mean over the four years subtracted. The results suggest that closer than 30° to the pole the rotation rate is time dependent, with the rotation less differential in 1990 than in 1986. Solar maximum was near 1990. The result of the inversion closer than 15° to the poles is not shown as the averaging kernels cannot be localized that close to the poles.

Acknowledgements

The authors are grateful for the opportunity to use the SOI-MDI, GONG, and BBSO data and acknowledge the effort of all of the teams involved in the collection and reduction of the data.

4.3 A Time-Distance Search for Longitudinal Structure [1]

Most current models predict that magnetic field generated and stored at the base of the convection zone plays an important role in the solar dynamo (e.g. Kosovichev, 1996b). There have not been, however, any widely accepted measurements of the magnetic field in the tachocline. Dziembowski & Goode (1989) and Dziembowski & Goode (1991) used normal-mode helioseismology with BBSO data and found a megagauss strength quadrapole toroidal magnetic field at the base of the convection zone. This result was, however, later suggested to be due to the inaccuracy of solar models in the tachocline (Gough & McIntyre, 1998). This problem can only be overcome by making a differential measurement of some sort. Time-distance helioseismology provides a nice way to do this by looking at variations with longitude, something that cannot be done using the normal-mode approach. By looking for longitudinal variations, any uncertainty in the solar model can be removed as long as it is axisymmetric, which all standard solar models are.

In addition, there are two reasons to suppose that there is a non-axisymmetric component to the magnetic field in the tachocline: the possible presence of "active longitudes" (Bai (1990) gives an introduction) and theoretical studies of the stability of the tachocline find that the most unstable modes are the $m = 1$ modes (e.g. Gilman & Fox, 1999). In order to study the non-axisymmetric components of the magnetic field it is necessary to do something besides standard normal mode helioseismology.

[1] *This section is based on unpublished work and is a result of collaboration with T. Duvall and A. G. Kosovichev. T. Duvall has been measuring the cross-correlations, and in some cases travel times as well. I have been working on the kernels, the inversions, and the comparison with surface magnetic field.*

For the above described reasons we have begun a first effort at detecting longitudinal variations in the deep convection zone. The primary result of this search is a rough upper limit of 0.8 MG on longitudinal variations in the magnetic field in the tachocline over Carrington rotations 1965, 1966, and 1967. A secondary result is that the effect of surface magnetic field is likely an important source of noise; future studies should be carefully designed to minimize the artifacts it can cause. Dziembowski & Goode (1997) discuss this issue for normal-mode helioseismology.

The outline for the remainder of section 4.3 is as follows. Section 4.3.1 describes the basic data and introduces the deep-focusing method. Section 4.3.2 discusses travel-time kernels for deep focusing. The inversion results are shown in section 4.3.4. Section 4.3.5 shows a simple model of the effect of spatially distributed surface magnetic field on the inversion. The final section, 4.3.6, makes the connection between the sound speed perturbations that we observe and the effect of magnetic field in the deep convection zone.

4.3.1 The Data and Deep Focusing

The basic data are time series of medium-l (Kosovichev et al., 1997) Dopplergrams measured with the MDI instrument over Carrington rotations 1965, 1966, and 1967. For each rotation thirty regions are tracked, removing both the effects of solid and differential rotation, for 2048 minutes. The centers of the regions are separated by 12° in Carrington longitude and each region covers approximately 130° degrees in latitude centered around the equator and approximately 140° in longitude.

Throughout this dissertation we have often referred to the two-point time-distance cross-correlation function. In practice observed cross-correlations are noisy, and a number of cross-correlations have to be averaged together to provide a clean signal from which travel times can meaningfully be measured. The standard technique, termed "shallow focusing", has been to average the cross-correlation functions over quadrants of an annulus, with one observation point in the cross-correlation always at the center of the annulus (e.g. Duvall et al., 1997). This technique is not ideal for probing the solar interior, as it produces travel-time kernels that are strongest at the solar surface at the center of the annulus.

A new technique, termed "deep focusing", is now being developed. The geometry is substantially more complicated than for the "shallow focusing" technique described in the previous paragraph. The motivation for the deep-focusing technique is to compute average cross-correlations that give travel times that have sensitivity that is large near some "focus points" in the solar interior.

In order to think qualitatively about the sensitivity kernel for a particular travel time, it is useful to think about the rays paths that connect the observations points of the cross-correlations that contribute to that travel time. This is because the travel-time sensitivity kernel can be visualized once the ray path is known (section 3.2).

In the deep-focusing approach, we want to use all of the rays that pass through the focus point. Figure 4.9 shows the geometry. The figure is cylindrically symmetric around the line $x = 0$, which connects the focus point to the center of the Sun. In deep focusing we only consider cross-correlations between pairs of observation points that are on opposite sides of the focus point. For a particular pair of observation points and a particular focus point we define Δ as the distance between the observation points and Δ' as the larger of the two observation point to focus point distances. For a particular focus point we compute the cross-correlation, averaged over all pairs of observation points with the same Δ and Δ', with $4.2^\circ < \Delta < 63.6^\circ$. We then average this result over an 11 by 21 grid of focus points that covers six degrees in latitude around the equator and twelve degrees in longitude. Finally, as we are interested only in sound speed we symmetrize in time lag. The result we denote by $C(\Delta, \Delta', t, \lambda)$. The time lag is t and the central Carrington longitude of the focus points is λ. Notice that in a spherically symmetric solar model (ignoring line-of-sight effects) the cross-correlation would be independent of Δ' and λ and only depend on total distance Δ and time lag t.

4.3.2 Measurement of Travel Times

From the azimuthally-averaged single-distance cross-correlations described in the previous section, we compute the deep-focusing cross-correlations, which we denote by $\bar{C}(r, t, \lambda)$. The focus radius is r, the time lag t, and the longitude λ. The deep-focusing cross-correlation is the sum of windowed and time-shifted single-distance

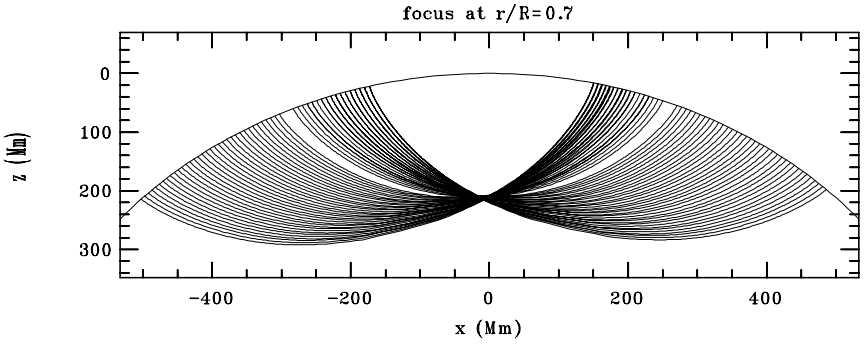

Figure 4.9: The ray paths used in the deep-focusing measurement. All of the ray paths pass through the focus point, which is at $r = 0.7R_\odot$. The figure is cylindrically symmetric around the line connecting the focus point with the center of the Sun. If the entire surface of the Sun were continuously observable then all rays that pass through the focus would be used. This figure is courtesy of T. Duvall.

cross-correlations

$$\bar{C}(r_k, t, \lambda) = \sum_{i=1}^{N} \sum_{j=1}^{M_i} a_{ij}^k f(t - t_i) C(\Delta_i, \Delta'_j, t - t_i, \lambda)\,. \tag{4.21}$$

The total number of distances is N. The number of distances Δ' is M_i, where the index i carries the dependence on total distance Δ_i. The window function is f and the t_i are the time shifts corresponding to each distance Δ_i. The time shifts are chosen so that the fine structure in the individual cross-correlations $C(\Delta_i, \Delta', t)$ add up coherently when shifted by the time lags t_i. For this work we choose the window function $f(t)$ to be one for $t < 10$ min and zero elsewhere. This choice was set by the temporal extent of the individual cross-correlations. The coefficients a_{ij}^k give the weight with which the cross-correlation at total distance Δ_i and annulus to focus point distance of Δ'_j contributes to the deep-focusing cross-correlation at focus radius r_k. For this work we take the a_{ij}^k to be either zero or one, though other schemes are possible. In particular we choose $a_{ij}^k = 1$ if the rays specified by (Δ_i, Δ'_j) pass through the focus point and are visible for the time duration of the

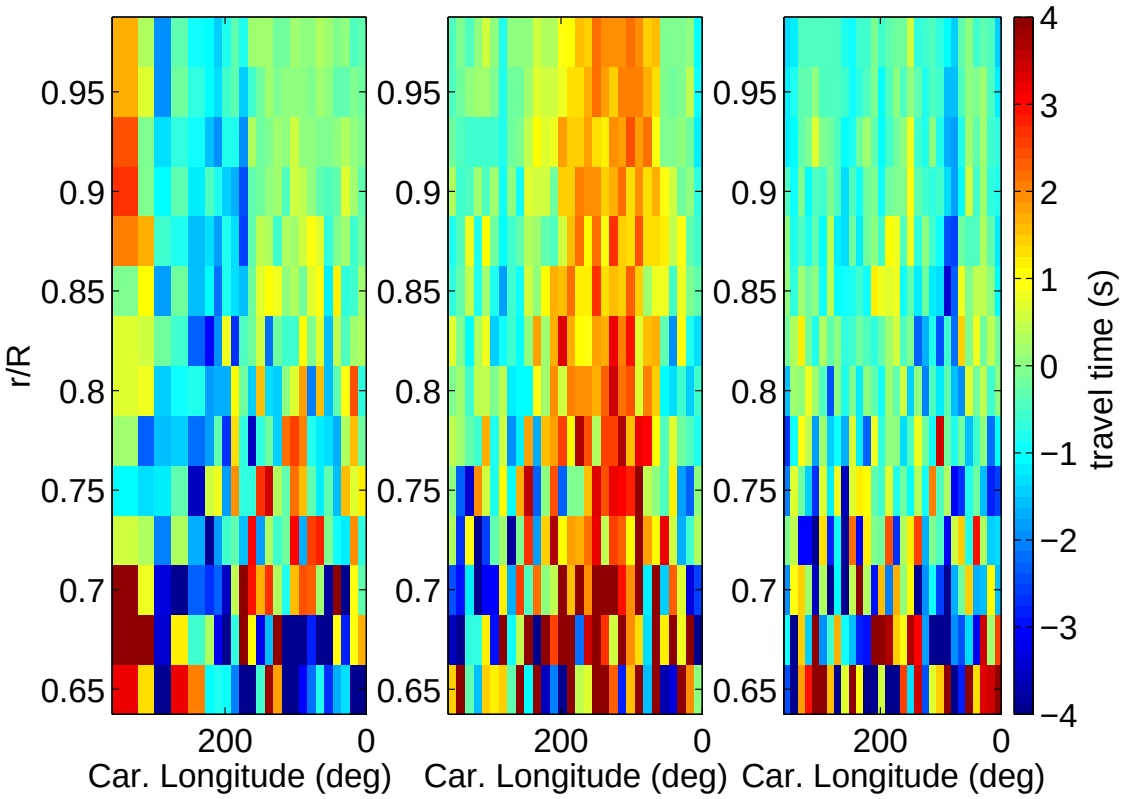

Figure 4.10: Deep-focusing travel time as a function of Carrington longitude and focus radius for Carrington rotations 1965,1966, and 1967 (from left to right). The color scale ranges from -4 seconds (blue) to +4 seconds (red).

observation, and $a_{ij}^k = 0$ otherwise.

We then measure travel times from the deep-focusing cross-correlations $\bar{C}(r, t, \lambda)$. We use the general approach of section 3.4.1 with the reference cross-correlations C^{ref} chosen to be the longitudinal averages of the observed deep-focusing cross-correlations. For a detailed description of the procedure see Appendix F.

The result of the travel-time measurement procedure is travel time as a function of focus radius and Carrington longitude, $\tau(r, \lambda)$. Figure 4.10 shows these travel times for Carrington rotations 1965,1966, and 1967. The dominant feature is that the travel time for Carrington longitudes 180 to 100 in rotation 1966 are larger than for other longitudes. This feature, however, is not clearly seen in either Carrington rotation 1965 or 1967.

The travel times for the shallowest and deepest focus depths are shown in Figure 4.11. It is clear that the deep-focusing travel times are not periodic (with a period of 360°), which would be expected if the Sun was not changing as it rotated. Also apparent from Figure 4.11 is that the errors in the travel times increase with focus depth. Figure 4.12 gives an estimate of the travel time error as a function of focus radius. This estimate was obtained by assuming that the small-scale (less than a few bins in longitude) scatter in the travel-time measurements is due entirely to noise. We would prefer to have a more meaningful noise estimate.

4.3.3 Travel-Time Kernels

We have travel time as a function of focus depth for thirty longitude bins for three Carrington rotations. In order to obtain a calculation that can be done in a reasonable amount of time, we make the assumption that we can do a separate one-dimensional (depth only) inversion for each longitude bin. This is a very rough approximation, as the longest rays that we use extend over five longitude bins. The sensitivity of the travel-time kernels should be largest, however, in the vicinity of the focus point, where all of the rays intersect. In the future we hope to be able to do true three-dimensional inversions.

In Appendix F we show a detailed derivation of deep-focusing travel-time kernels for sound speed, in the approximation that the sound speed perturbation is only a function of radius. The result of the calculation is travel-time kernels $K(r_{\rm focus}; r)$ which satisfy

$$\delta\tau(r_{\rm focus}) = \int_0^{R_\odot} {\rm d}r \; K(r_{\rm focus}; r) \frac{\delta c(r)}{c(r)} \,. \tag{4.22}$$

Here $\delta c(r)/c(r)$ is the fractional perturbation to sound speed as a function of radius. When doing inversions it is convenient to use a grid that is uniform in acoustic depth, defined as

$$t(r) = \int_r^{R_\odot} \frac{{\rm d}r'}{c(r')} \,. \tag{4.23}$$

There is potential for a confusion of notation with the time lag t. It should always be clear from context though which meaning of t is intended. With the change of

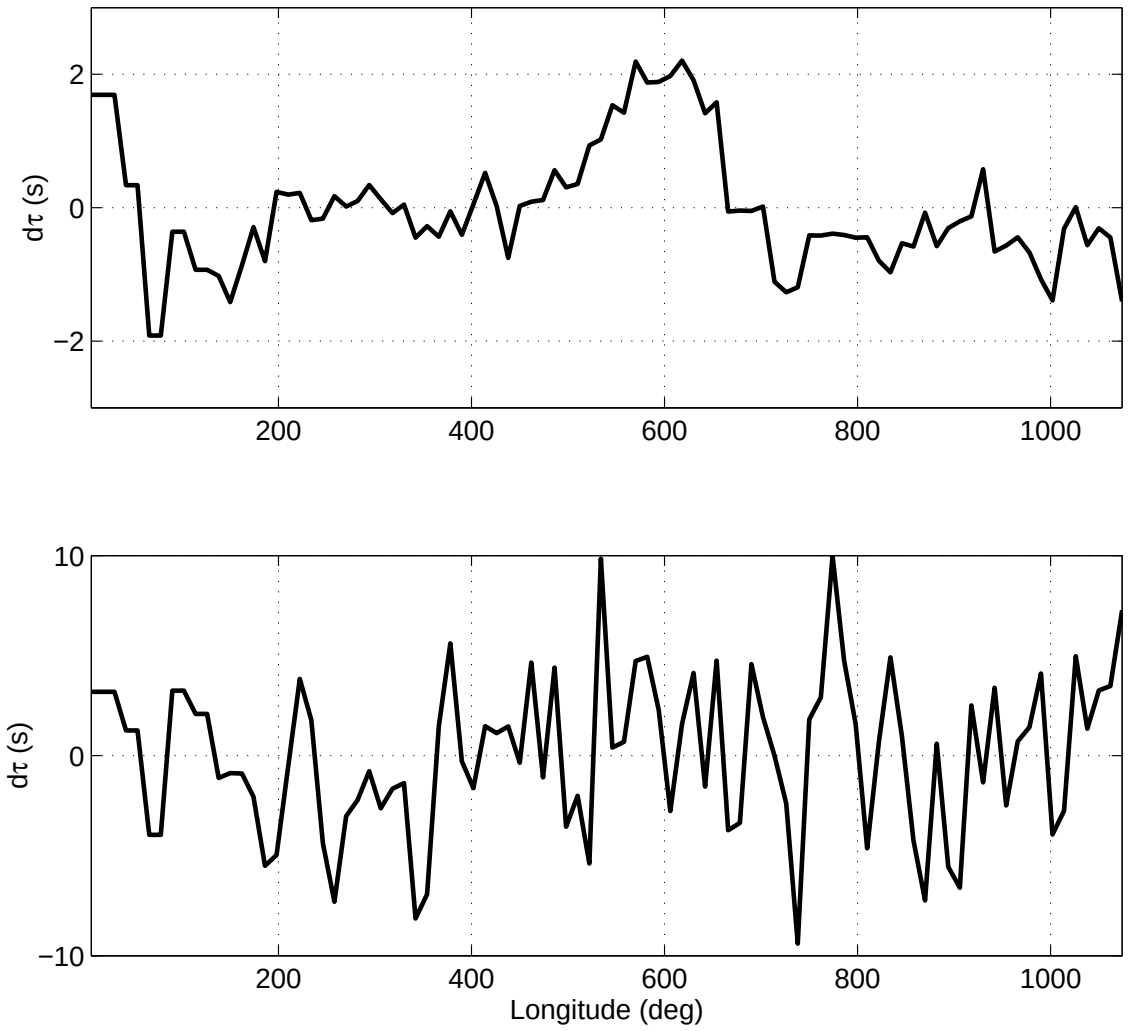

Figure 4.11: Deep-focus travel times for the shallowest (top panel) and deepest (lower panel) focus depths. In both panels the horizontal axis is degrees Carrington longitude since Carrington longitude 360° of rotation 1966. Notice the large feature at around longitude 600° in the top panel. If nothing were changing on the Sun, these plots would be periodic with a period of 360°.

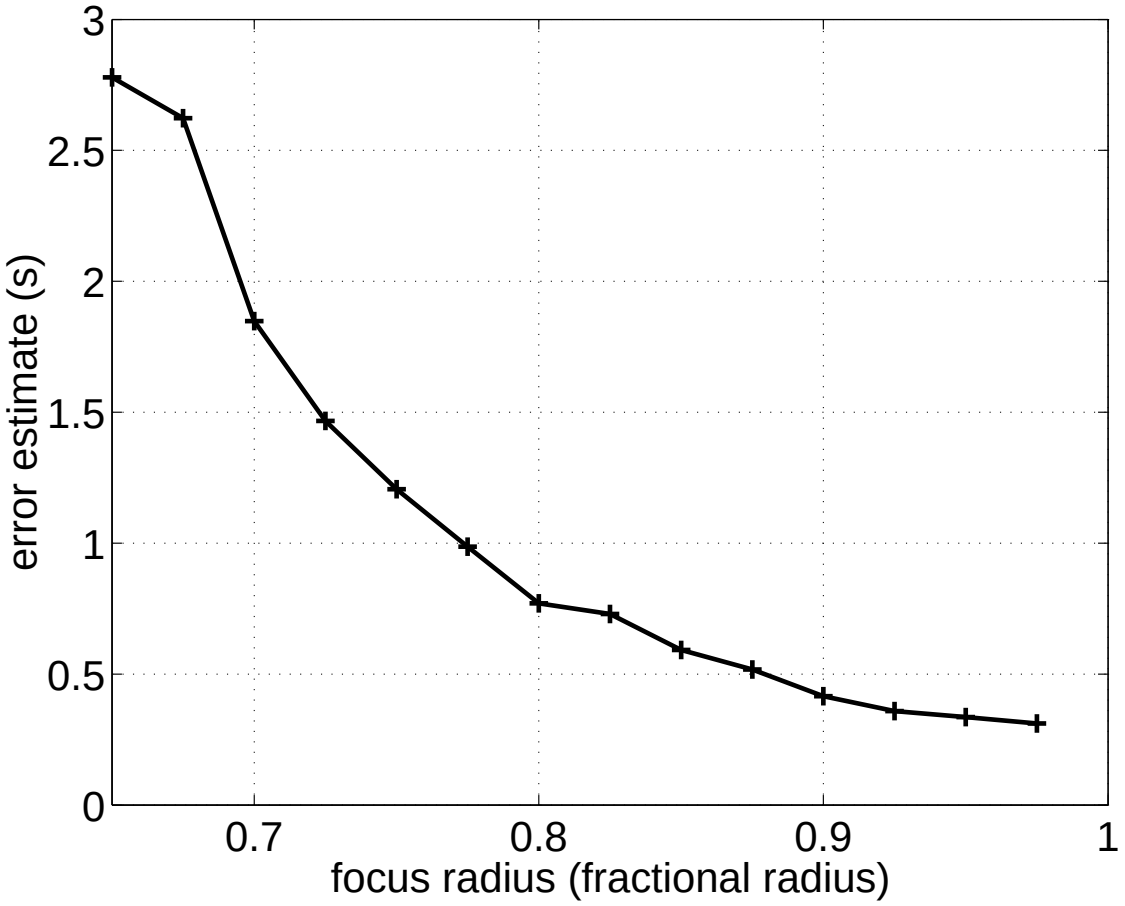

Figure 4.12: An estimate of the error in the deep-focusing travel times, shown in Figure 4.10, as a function of radius of the focus point. Note that the error increases rapidly with focus depth. These error estimates were obtained by assuming that the high spatial frequency part of the travel-time signal was noise. In the future we hope to use a more correct approach.

variable $r \to t(r)$ in equation (4.22) we obtain

$$\delta\tau(r_{\rm focus}) = \int_0^{t_{\rm max}} {\rm d}t\ \tilde{K}(r_{\rm focus}; t)\frac{\delta c(t)}{c(t)}\,. \tag{4.24}$$

In the above equation $t_{\rm max} = t(r = 0)$ is the acoustic depth of the center of the Sun, $t_{\rm max} \approx 60$ min, and $\tilde{K} = cK$.

Some sample kernels $\tilde{K}$ are shown in Figure 4.13. The kernels are in most places negative, indicating that an increase in sound speed leads to a decrease in travel time. The kernels are largest near the surface and near the focus depth. That the kernels have substantial weight near their focus depths shows that the deep-focusing procedure does in fact produce a travel time that is sensitive to the sound speed at the focus depth. As with all time-distance studies, the near-surface plays a role as well.

4.3.4 OLA Inversion

The OLA inversion we do exactly as in section 4.1. The data are the observed travel times. We use the kernels $\tilde{K}$ described in the previous section. The error estimates are shown in Figure 4.12. In order to choose the regularization parameter α we look at the trade-off between error magnification and the spreading of the averaging kernels. To measure the error magnification we use the second term in equation (4.5)

$$E = \sum_i a_{ij}^2 \sigma_i^2\,. \tag{4.25}$$

To measure the spreading of the kernels we use the first part

$$S = \int_0^{t_{\rm max}} {\rm d}t\ W(t - t_{\rm focus})\kappa^2(t)\,. \tag{4.26}$$

In the above equation the integration variable t is acoustic depth. The weight function is $W(t) = t^2$. The averaging kernel is given by κ. Figure 4.14 shows the trade-off between E and S as the regularization parameter α is changed. For the remainder of this work we use the value of the regularization parameter corresponding to the circle in Figure 4.14.

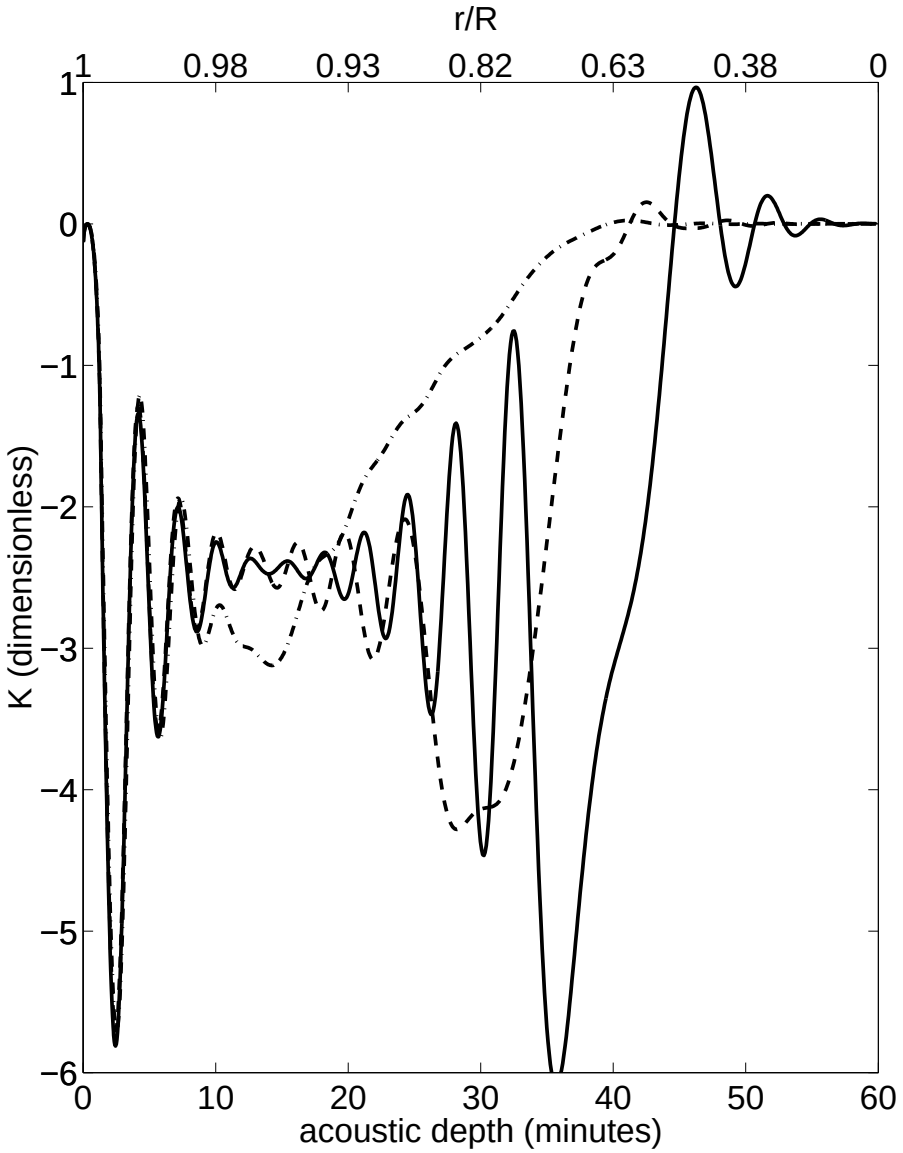

Figure 4.13: Deep-focusing travel-time kernels, $\tilde{K}$, for sound speed. The solid line is for a focus depth of $0.65R_\odot$(39 min), the dashed line is for $0.8R_\odot$(31 min), and the dot-dashed line is for $0.975R_\odot$(13 min). The lower horizontal axis is acoustic depth, in minutes. The upper horizontal axis is fractional radius. An acoustic depth of 60 min corresponds to the center of the Sun and 0 to the solar surface. Notice that all three of the kernels are similar near the surface (small acoustic depth). The kernels are mostly negative, i.e. an increase in sound speed leads to decreased travel time. Also notice that the kernel for the deepest focus depth (solid line) has weight at greater depth than the other two.

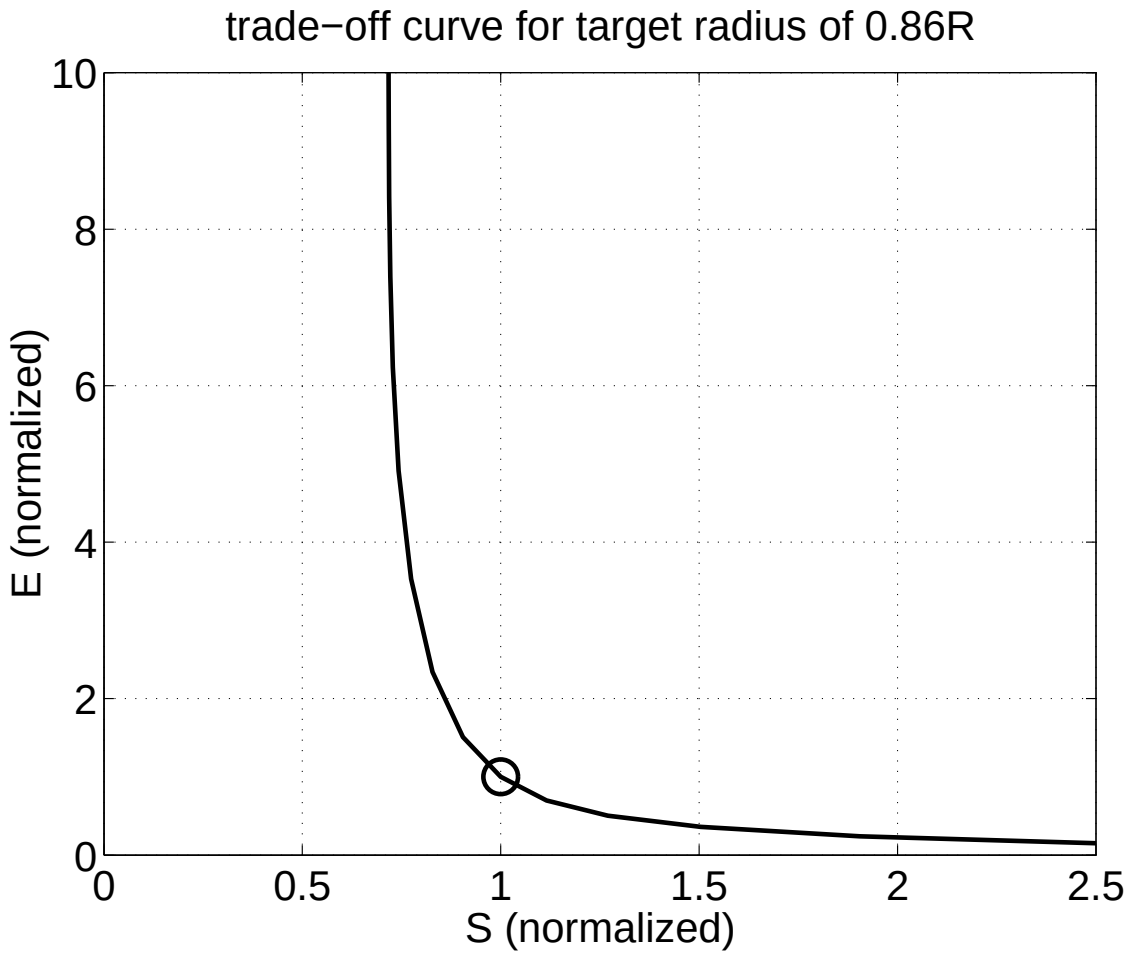

Figure 4.14: The relationship between error magnification (vertical axis) and spreading of the averaging kernel (horizontal axis) as the regularization parameter α is varied. Both axes have been scaled so that $E(\alpha_0) = S(\alpha_0) = 1$ where α_0 is the regularization parameter we have chosen for this study. This plot is for the averaging kernel for fractional sound speed at $r = 0.86R_\odot$. For large α the error magnification is small but the averaging kernels are not well localized. For small α the error magnification is large but the kernels are well localized.

The result of the OLA inversion, which gives an estimate of the fractional sound speed perturbation as a function of depth and Carrington longitude, is shown in Figure 4.15. Were the Sun constant in time, the sound speed inversion would be periodic with a period of 360°, this is clearly not the case in Figure 4.15. The interpretation of the inversion result is not totally straightforward, as we will see in the next section.

4.3.5 Effect of Surface Magnetic Field

It is well known that surface magnetic field correlates with the travel times of wave packets (e.g. Lindsey & Braun, 2000). The physical mechanism is not, however, known. We would like to investigate whether the inversion result that we have obtained (Fig. 4.15) can be explained solely as an artifact of near-surface magnetic field. In order to test this hypothesis we made a set of artificial travel times, $\tau_B(r_{\rm focus}, \lambda)$, with the assumption that

$$\tau_B(r_{\rm focus}, \lambda) = -\int \mathrm{d}\boldsymbol{x}\, F(\boldsymbol{x}; r_{\rm focus}, \lambda)|B(x)|\,. \tag{4.27}$$

In the above equation B is the MDI magnetic field. The integral $\int \mathrm{d}\boldsymbol{x}$ is taken over the surface of the Sun. The spatial weighting function $F(\boldsymbol{x}; r_{\rm focus}, \lambda)$ is the density of observation points for the cross-correlations used in the deep focusing average with focus radius $r_{\rm focus}$ and longitude λ. Figure 4.16 shows some sample weight functions F. The essential point is that the weight functions depend on focus depth. As a result, given a non-uniform spatial distribution of magnetic field, the travel times τ_B will depend on focus depth. A near surface effect, however, gives deep-focus travel times that are independent of focus depth (in Figure 4.13 notice that the kernels are identical near the surface).

Figure 4.17 shows the result of inverting the travel times τ_B. The overall amplitude has been scaled to give results of the same magnitude as the inversion shown in Figure 4.15. There are two main features in the inversion of τ_B. The first is that what is nominally a surface effect has leaked down to a radius of $0.95R_\odot$, this is not surprising and merely reflects the near-surface resolution of the data, which we confirmed by inverting a set of travel times $\tau(r_{\rm focus}, \lambda) = 1$. The second, and

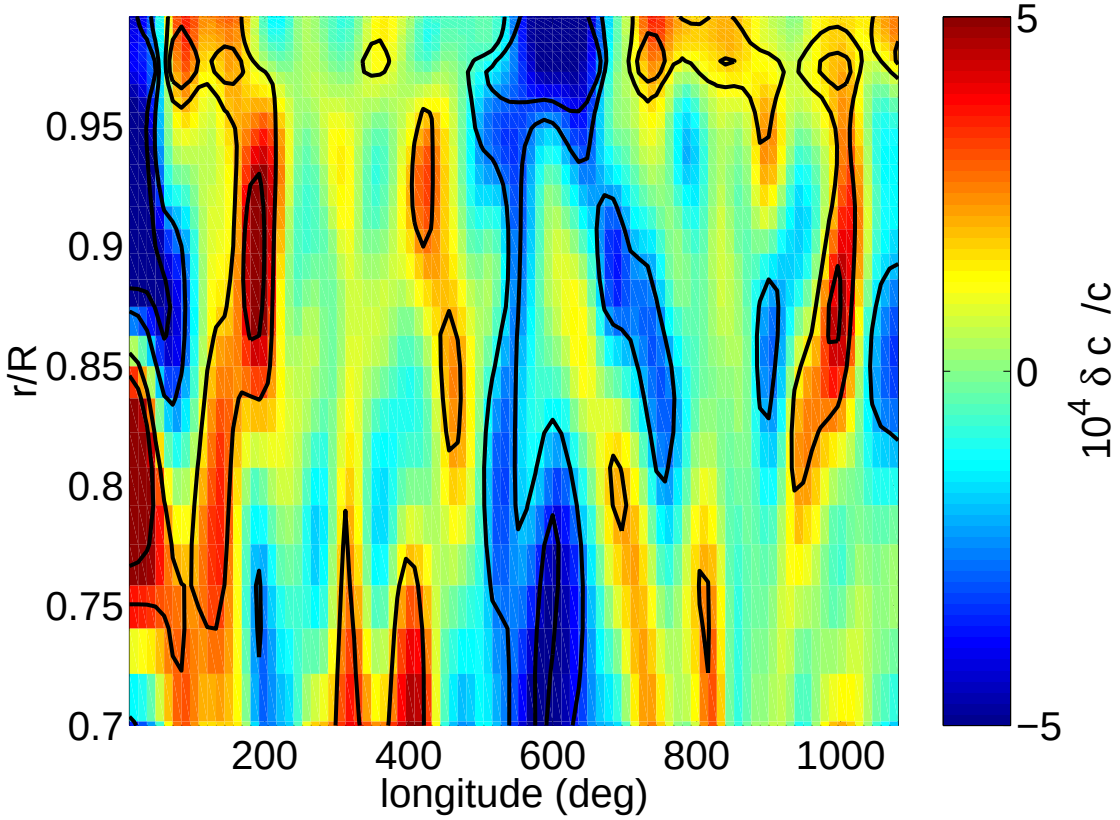

Figure 4.15: Result of OLA inversion for sound speed as a function of depth and Carrington longitude for rotations 1965, 1966, and 1967. The horizontal axis is degrees Carrington longitude since Carrington Longitude 360° of rotation 1965 arranged so that time runs continuously to the right. The vertical axis is fractional radius and the color scale denotes the value of the fractional sound speed perturbation. The color scale runs from -8×10^{-4} (blue) to 4.5×10^{-4} (red). The contour lines show the regions that are further than 2σ and 4σ from zero. The inversion has been smoothed in longitude with a Gaussian filter with HWHM of 10° .

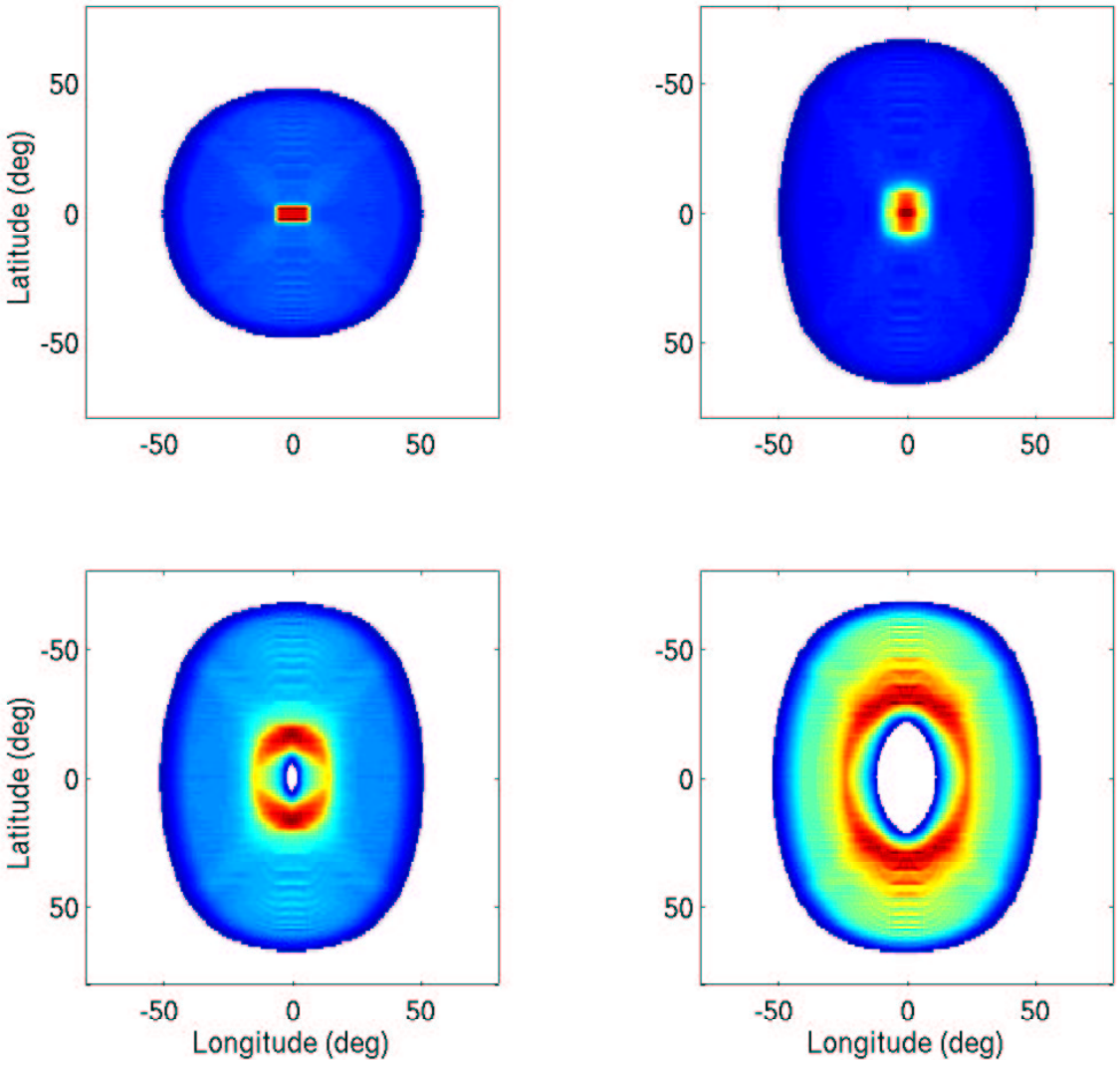

Figure 4.16: Spatial weights for averaging the surface magnetic field. The top left panel is for a focus radius of $0.975R_\odot$, the top right for $0.875R_\odot$, the bottom left for $0.75R_\odot$, and the bottom right for $0.65R_\odot$. The color scale indicates the value of the weight functions, with red largest, blue smallest, and white zero. Notice as the fractional radius of the focus depth decrease, the weights become zero for small distances. This is because the deep focus depths cannot use cross-correlations between points separated by small distances.

much more interesting feature, is that the inversion of τ_B shows features in the deep convection zone, of the same magnitude as the near-surface features. This result shows that the horizontal variation in the surface magnetic field causes features at depth in the inversion. As a result we must be very cautious about interpreting the original inversion result (Fig. 4.15).

Figures 4.17 and 4.15 are not, however, identical. There are several possible causes. Perhaps there are in fact sound speed perturbations at depth. This possibility can not be ruled out by the current analysis. Another possibility is that the spatial weights F that we have employed are not sufficiently accurate. In particular, we did not take account of the distance dependence of the weight with which individual cross-correlations contribute to the deep-focusing average. A more detailed calculation would be a serious undertaking, and beyond the scope of this first attempt.

4.3.6 Interpretation in Terms of Deep Magnetic Field

Thus far we have only obtained inversions for fractional sound speed perturbations. We would like, however, to use these results to make some estimates about the possible strength of longitudinal variations in the magnetic field in the deep convection zone. We expect that the magnetic field will appear in inversions for sound speed both by the direct mechanical effect of the magnetic field on the wave speed (Kosovichev & Duvall, 1997) and by the effect of magnetic field on the stratification of the convection zone. A detailed calculation of the effect of magnetic field on time-distance measurements has not yet been done. In order to obtain a rough estimate of the magnetic field variations in the deep convection zone, we assume that the dominant effect of magnetic field is to increase the square of the sound speed by the square of the local Alfvén speed (i.e. wave packets move at the fast-mode speed)

$$\delta c^2 = B^2/4\pi\rho\,. \tag{4.28}$$

With this assumption, a fractional sound speed perturbation of 5×10^{-4} at the base of the convection zone, where $\rho = 0.2\,\mathrm{gm\,s^{-3}}$ and $c^2 = 5.2\times10^{14}\,\mathrm{cm^2\,s^{-2}}$, gives an estimate for B of 0.8 MG.

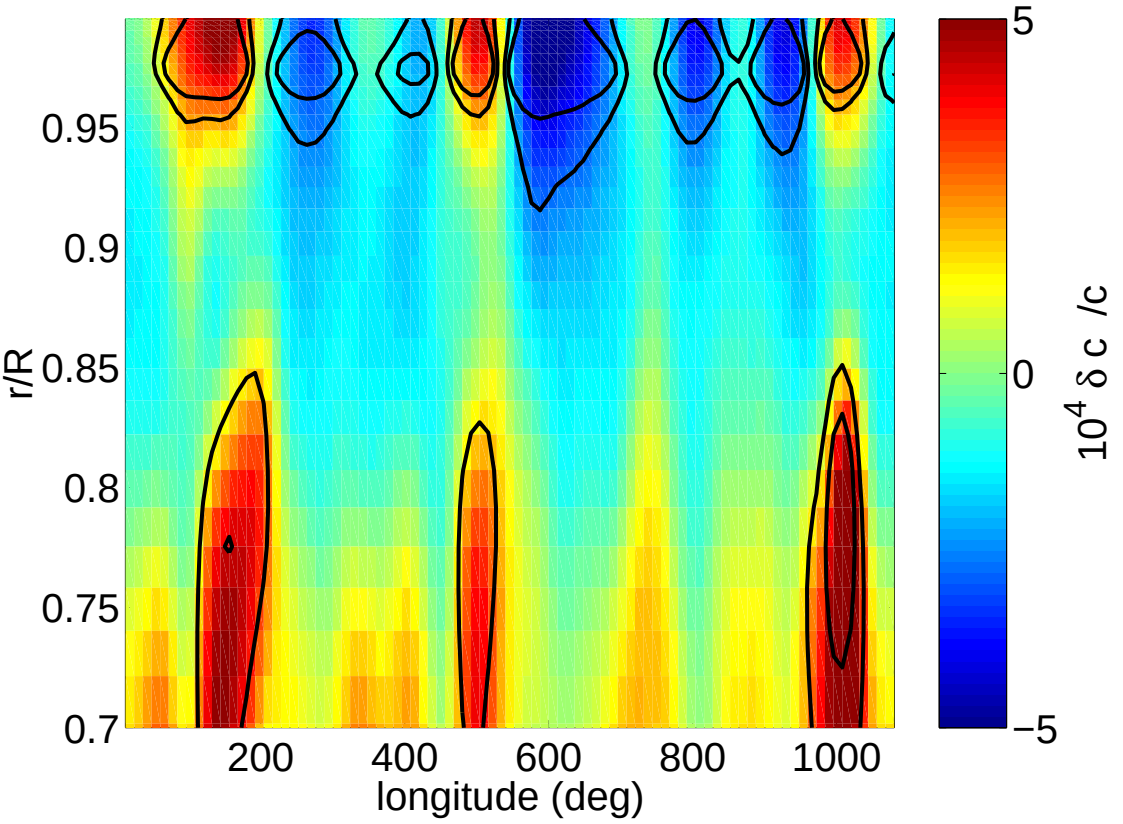

Figure 4.17: Effect of surface magnetic field on the inversion. For this figure, we assume that travel time is proportional to the spatial average of the magnetic field (eq.[4.27]). These travel times are then inverted, using the same inversion technique as for Figure 4.15. The near surface effects are expected, travel times are known to be decreased underneath magnetic regions (e.g. Lindsey & Braun, 2000). Artifacts, however, appear in the deep convection zone as a result of the focus depth dependence of the spatial averaging of the surface magnetic field.

A field strength of 0.8 MG. is substantially larger than one might expect given the results of the recent simulations of rising magnetic flux tubes by Fan et al. (1994). They find that flux tubes with field strengths of 10 to 100 kG emerge at latitudes compatible with the observed active latitudes. By extrapolation of their results to very high field strength, it would appear that flux tubes with strengths of $0.8MG$ emerge at essentially the same latitude as they have in the tachocline. In particular, tubes leaving the tachocline at the equator would emerge at the surface at the equator. There is, however, very little magnetic field seen at the equator. The resolution of this puzzle is not at all clear, and there clearly remains a substantial amount of work to be done on this subject.